

Slow-light enhanced subwavelength plasmonic waveguide refractive index sensors

Yin Huang,^{1,*} Changjun Min,² Pouya Dastmalchi,^{3,4} and Georgios Veronis^{3,4}

¹*Department of optoelectrics information science and engineering, School of Physics and Electronics, Central South University, Changsha, Hunan 410012, China*

²*Institute of Micro-Nano Optics, Key Laboratory of Optoelectronic Devices and Systems of Ministry of Education and Guangdong Province, College of Optoelectronic Engineering, Shenzhen University, Shenzhen 518060, China*

³*Department of Electrical and Computer Engineering, Louisiana State University, Baton Rouge, Louisiana 70803, USA*

⁴*Center for Computation and Technology, Louisiana State University, Baton Rouge, Louisiana 70803, USA*

[*yhuan15@csu.edu.cn](mailto:yhuan15@csu.edu.cn)

Abstract: We introduce slow-light enhanced subwavelength scale refractive index sensors which consist of a plasmonic metal-dielectric-metal (MDM) waveguide based slow-light system sandwiched between two conventional MDM waveguides. We first consider a MDM waveguide with small width structure for comparison, and then consider two MDM waveguide based slow light systems: a MDM waveguide side-coupled to arrays of stub resonators system and a MDM waveguide side-coupled to arrays of double-stub resonators system. We find that, as the group velocity decreases, the sensitivity of the effective index of the waveguide mode to variations of the refractive index of the fluid filling the sensors as well as the sensitivities of the reflection and transmission coefficients of the waveguide mode increase. The sensing characteristics of the slow-light waveguide based sensor structures are systematically analyzed. We show that the slow-light enhanced sensors lead to not only 3.9 and 3.5 times enhancements in the refractive index sensitivity, and therefore in the minimum detectable refractive index change, but also to 2 and 3 times reductions in the required sensing length, respectively, compared to a sensor using a MDM waveguide with small width structure.

© 2015 Optical Society of America

OCIS codes: (240.6680) Surface plasmons; (130.2790) Guided waves; (130.6010) Sensors.

References and links

1. W. L. Barnes, A. Dereux, and T. W. Ebbesen, "Surface plasmon subwavelength optics," *Nature* **424**, 824–830 (2003).
2. F. Hao, P. Nordlander, Y. Sonnefraud, P. van Dorpe, and S. A. Maier, "Tunability of Subradiant Dipolar and Fano-Type Plasmon Resonances in Metallic Ring/Disk Cavities: Implications for Nanoscale Optical Sensing," *ACS Nano* **3**,(3) 643–652 (2009).
3. N. Liu, T. Weiss, M. Msche, L. Langguth, U. Eigenthaler, M. Hirscher, C. Sonnichsen, and H. Giessen, "Planar metamaterial analogue of electromagnetically induced transparency for plasmonic sensing," *Nature* **10**, 1103–1107 (2010)

4. Y. Gao, Q. Gan, Z. Xin, X. Cheng, and F. J. Bartoli, "Plasmonic Mach-Zehnder Interferometer for Ultrasensitive On-Chip Biosensing," *ACS Nano* **5**, 9836–9844 (2011).
5. Y. H. Fu, J. B. Zhang, Y. F. Yu, and B. Luk'yanchuk, "Generating and Manipulating Higher Order Fano Resonances in Dual-Disk Ring Plasmonic Nanostructures," *ACS Nano* **6**,(6) 5130–5137 (2012).
6. F. Fan, S. Chen, X. H. Wang, and S. J. Chang, "Tunable nonreciprocal terahertz transmission and enhancement based on metal/magneto-optic plasmonic lens," *Opt. Express* **21**(7), 8614–8621 (2013).
7. J. H. Zhou, X. P. Xu, W. B. Han, D. Mu, H. Song, Y. Meng, X. Leng, J. Yang, X. Di, and Q. Chang, "Fano resonance of nanoparticles embedded in Fabry-Perot cavities," *Opt. Express* **21**(10), 12159–12164 (2013).
8. A. G. Brolo, "Plasmonics for future biosensor," *Nat. Photon.* **6**, 709–713 (2012).
9. Z. Yu, G. Veronis, S. Fan, and M. L. Brongersma, "Gain-induced switching in metal-dielectric-metal plasmonic waveguides," *Appl. Phys. Lett.* **92**, 041117 (2008).
10. C. Min and G. Veronis, "Absorption switches in metal-dielectric-metal plasmonic waveguides," *Opt. Express* **16**, 10757–10766 (2009).
11. W. Cai, J. S. White, and M. L. Brongersma, "Compact, high-speed and power-efficient electro-optic plasmonic modulators," *Nano Lett.* **9**, 4403–4411 (2009).
12. D. K. Gramotnev and S. I. Bozhevolnyi, "Plasmonics beyond the diffraction limit," *Nat. Photon.* **4**, 83–91 (2010).
13. G. Zhan, R. Liang, H. Liang, J. Luo and R. Zhao, "Asymmetric band-pass plasmonic nanodisk filter with mode inhibition and spectrally splitting capabilities," *Opt. Express* **22**, 9912–9919 (2014).
14. T. Wu, Y. Liu, Z. Yu, Y. Peng, C. Shu and H. Ye, "The sensing characteristics of plasmonic waveguide with a ring resonator," *Opt. Express* **22**, 7669–7677 (2014).
15. E. N. Economou, "Surface plasmons in thin films," *Phys. Rev.* **182**, 539–554 (1969).
16. A. Karalis, E. Lidorikis, M. Ibanescu, J. Joannopoulos, and M. Soljacic, "Surface-plasmon-assisted guiding of broadband slow and subwavelength light in air," *Phys. Rev. Lett.* **95**, 063901 (2005).
17. M. Sandtke and L. Kuipers, "Slow guided surface plasmons at telecom frequencies," *Nat. Photon.* **1**, 573 (2007).
18. Q. Gan, Y. J. Ding, and F. J. Bartoli, "'Rainbow' trapping and releasing at telecommunication wavelengths," *Phys. Rev. Lett.* **102**, 056801 (2009).
19. L. Yang, C. Min, and G. Veronis, "Guided subwavelength slow-light mode supported by a plasmonic waveguide system," *Opt. Lett.* **35**, 4184–4186 (2010).
20. Y. Huang, C. Min, and G. Veronis, "Subwavelength slow-light waveguides based on a plasmonic analogue of electromagnetically induced transparencies," *Appl. Phys. Lett.* **99**, 143117 (2011).
21. P. Berini, "Bulk and surface sensitivities of surface plasmon waveguides," *New J. Phys.* **10**, 105010 (2008).
22. S. D. Wu, and E. N. Glytsis, "Finite-number-of-periods holographic gratings with finite-width incident beams: analysis using the finite-difference frequency-domain method," *J. Opt. Soc. Am.* **65**, 2018–2029 (2002).
23. G. Veronis, R. W. Dutton, and S. Fan, "Method for sensitivity analysis of photonic crystal devices," *Opt. Lett.* **29**, 2288–2290 (2004).
24. *Handbook of Optical Constants of Solids*, edited by E. D. Palik (Academic, 1985).
25. J. Jin, *The Finite Element Method in Electromagnetics*, (Wiley, 2002).
26. A. Melikyan, L. Alloati, A. Muslija, D. Hillerkuss, P. C. Schindler, J. Li, R. Palmer, D. Korn, S. Muehlbrandt, D. Van Thourhout, B. Chen, R. Dinu, M. Sommer, C. Koos, M. Kohl, W. Freude and J. Leuthold, "High-speed plasmonic phase modulators," *Nat. Photon.* **9**, 229–234 (2014).
27. Y. Zhu, X. Hu, H. Yang and Q. Gong, "On-chip plasmon-induced transparency based on plasmonic coupled nanocavities," *Sci. Rep.* **4**, 3752–3758 (2014).
28. S. E. Kocabas, G. Veronis, D. A. B. Miller, and S. Fan, "Transmission line and equivalent circuit models for plasmonic waveguide components," *IEEE J. Sel. Topics Quantum Electron.* **14**, 1462–1472 (2008).
29. Y. Huang, C. Min and G. Veronis, "Compact slit-based couplers for metal-dielectric-metal plasmonic waveguides," *Opt. Express* **20**, 22233–22244 (2012).
30. A. Taflov, *Computational Electrodynamics*, (Artech House, Boston, 1995).
31. J. Joannopoulos, S. Johnson, J. Winn and R. Meade, *Molding the Flow of Light*, (Princeton University Press, 2008).
32. G. Cao, H. Li, S. Zhan, H. Xu, Z. Liu, Z. He and Y. Wang, "Formation and evolution mechanisms of plasmon-induced transparency in MDM waveguide with two stub resonators," *Opt. Express* **21**, 9198–9205 (2013).
33. K. Dignonnet, H. Wen, M. Terrel, Y. Huo and S. Fan, "Slow light in fiber sensors," *Proc. SPIE.* **8273**, 82730W1 (2012).
34. K. C. Huang, M. Seo, T. Sarmiento, Y. Huo, J. S. Harris and M. L. Brongersma, "Electrically driven subwavelength optical nanocircuits," *Nat. Photon.* **8**, 244–249 (2014).
35. Y. Fu, X. Hu, C. Lu, S. Yue, H. Yang and Q. Gong, "All-Optical Logic Gates Based on Nanoscale Plasmonic Slot Waveguides," *Nano. Lett.* **12**, 5784–5790 (2012).
36. D. M. Pozar, *Microwave Engineering*, (Wiley, 1998).
37. Y. Zhao, Y. Zhang and Q. Wang, "High sensitivity gas sensing method based on slow light in photonic crystal waveguide," *Sens. Actuator. B. Chem.* **173**, 28–31 (2012).

1. Introduction

The unique properties of surface plasmons, which are light waves that propagate along metal surfaces, enable a wide range of practical applications, including light guiding and manipulation at the nanoscale [1]. In recent years, surface plasmon resonance (SPR) based sensors have been widely employed and investigated [2–7], especially the refractive index (RI) sensing. Both propagating surface plasmon resonances (PSPRs) and localized surface plasmon resonances (LSPRs) exhibit great potentials for sensing applications due to their susceptibility to the changes in the RI of the surrounding environment [8]. Among different plasmonic waveguiding structures, metal-dielectric-metal (MDM) plasmonic waveguides are of particular interest [9–14], because they support modes with deep subwavelength scale over a very wide range of frequencies extending from DC to visible, and are relatively easy to fabricate [15]. In a MDM waveguide the modal fields are highly confined in the dielectric region. This characteristic also makes the MDM waveguides very attractive for sensing applications. In addition, slow light offers the opportunity for compressing the local optical energy density, which enhances light-matter interactions, and thereby improves the performance of nanoscale plasmonic devices [16–20]. Therefore, it is essential to investigate the sensing characteristics of plasmonic MDM waveguide based slow-light RI sensors.

In this paper, we investigate RI sensors consisting of a plasmonic slow-light waveguide sandwiched between two conventional MDM waveguides. In these structures, light is coupled from an input MDM plasmonic waveguide to a plasmonic slow-light waveguide system, and then coupled back to an output MDM plasmonic waveguide. We first consider a MDM waveguide with small width as the plasmonic waveguide sensing system. We next consider two different plasmonic slow-light waveguide sensing systems: the MDM waveguide side-coupled to arrays of MDM stub resonators system [19] and the MDM waveguide side-coupled to arrays of MDM double-stub resonators system [20]. We find that, decreased group velocity v_g in slow-light systems significantly enhances not only the sensitivity of the effective index of optical mode to variations of the refractive index of the fluid filling in the sensors, but also the sensitivities of the transmission and reflection coefficients to variations of the RI of the fluid. The two optimized slow-light enhanced subwavelength plasmonic RI sensors result in not only 3.9 and 3.5 times enhancements in the sensitivity, and therefore in the minimum detectable RI change, but also 2 and 3 times reductions in the optimal sensing length, respectively, compared to a sensor using a MDM waveguide with small width system. Although the two optimized slow-light enhanced sensors have comparable performance in sensitivity, the double-stub resonator system exhibits a small group velocity dispersion over a broader wavelength range and has less power loss, features which are highly desirable for practical sensing applications.

The remainder of the paper is organized as follows. In Section 2, we first define the figure of merit for a given sensing system and briefly describe the simulation method used for the analysis of the sensors. The results obtained for the conventional MDM waveguide with small width, MDM waveguide side coupled to stubs and MDM waveguide side coupled to double stubs systems are presented in Subsections 2.1, 2.2 and 2.3, respectively. Finally, our conclusions are summarized in Section 3.

2. Results

For application of ultradense chip-scale integration, we consider compact subwavelength scale RI sensor. In all cases, the total length of the sensing structure is limited to less than $1.1\ \mu\text{m}$, which approximately corresponds to one wavelength in water ($\lambda_w = \lambda_0/n_w$, where $n_w = 1.332$), when operating at the optical communication wavelength ($\lambda_0 = 1.55\ \mu\text{m}$). To characterize the sensing capability of the proposed sensors, we define the following *figure of merit (FOM)* in

terms of the relative change in the output power that occurs for a change in the RI

$$FOM = \frac{1}{P_{in}} \left| \frac{dP_{out}(n)}{dn} \right| = \left| \frac{dT(n)}{dn} \right| \quad (1)$$

where n is the RI of fluid and $T = \frac{P_{out}}{P_{in}}$ is the power transmission. The input power P_{in} is given as a constant. The output power P_{out} is the only measurable quantity in such a sensor. The changes in P_{out} are related to Δn via $\Delta P_{out} = \frac{dP_{out}(n)}{dn} \Delta n$ [21]. Denoting the smallest measurable change in output power as $\Delta P_{out,min}$, we obtain following expression for the detection limit Δn_{min} of the sensor

$$|\Delta n_{min}| = \frac{1}{P_{in}} \left| \frac{\Delta P_{out,min}}{FOM} \right| \quad (2)$$

It is noted that the detection limit $|\Delta n_{min}|$ decreases as the FOM increases.

We use a two-dimensional finite-difference frequency-domain (FDFD) method [22, 23] to numerically calculate the transmission in the MDM plasmonic waveguide. This method allows us to directly use experimental data for the frequency-dependent dielectric constant of metals such as silver [24], including both the real and imaginary parts, with no approximation. Perfectly matched layer (PML) absorbing boundary conditions are used at all boundaries of the simulation domain [25].

2.1. MDM waveguide with small width structure

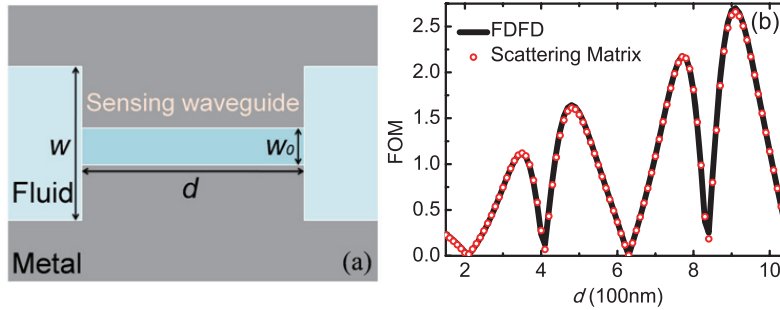


Fig. 1. (a) Schematic of the plasmonic RI sensor structure consisting of a MDM waveguide with small width sandwiched between two MDM waveguides. (b) FOM for the structure of Fig. 1(a) as a function of the sensing length d calculated using FDFD (black solid line) and scattering matrix theory (red circles). Results are shown for $w = 140$ nm and $w_0 = 50$ nm at $\lambda = 1.55$ μm . The metal is silver and the fluid is water.

We first consider a RI sensor consisting of a MDM waveguide with small width sandwiched between two conventional MDM waveguides (Fig. 1(a)). The width of the sensing MDM waveguide is $w_0 = 50$ nm. Since MDM waveguides with width $w \cong 140$ nm were used to guide optical mode in several plasmonic nanocircuits both theoretically and experimentally [26, 27], here the widths of input and output waveguides are also set to be $w = 140$ nm. All of the MDM waveguides in this structure (Fig. 1(a)) have subwavelength widths, so that only the fundamental TM mode is propagating in them. Thus, we can use single-mode scattering matrix theory to account for the behavior of the system [28, 29]. We use FDFD to extract the complex magnetic field reflection coefficient r_1 and transmission coefficient t_1 of the fundamental mode of a MDM waveguide at the input interface between the two MDM waveguides with different width (Fig. 2(a)), as well as the reflection coefficient r_2 and transmission coefficient t_2 at the output interface (Fig. 2(b)).

The *FOM* of the sensor structure of Fig. 1(a) can then be calculated using scattering matrix theory as: [28, 29]

$$FOM = |e^{-2A}[(C_\alpha \frac{dA}{dn} + C_\beta \frac{dB}{dn}) + C_T \frac{d|t_1 t_2|^2}{dn} + (C_a \frac{da}{dn} + C_b \frac{db}{dn})]|, \quad (3)$$

where

$$C_\alpha = \frac{2|t_1 t_2|^2[(a^2 + b^2)e^{-4A} - 1]}{\eta^2}, \quad (4)$$

$$C_\beta = \frac{4e^{-4A}|t_1 t_2|^2[b \cos(2B) - A \sin(2A)]}{\eta^2}, \quad (5)$$

$$C_T = \frac{1}{\eta}, \quad (6)$$

$$C_a = \frac{2e^{-2A}|t_1 t_2|^2[\cos(2B) - be^{-2A}]}{\eta^2}, \quad (7)$$

$$C_b = \frac{2e^{-2A}|t_1 t_2|^2[\sin(2B) - ae^{-2A}]}{\eta^2}, \quad (8)$$

and the coefficient η is defined as follow

$$\eta = |1 - r_2^2 e^{-2\gamma d}|^2 = 1 - 2ae^{-2A} \cos(2B) - 2be^{-2B} \cos(2B) + (a^2 + b^2)e^{-4A}, \quad (9)$$

where $\gamma = \alpha + i\beta$ is the complex wave vector of the fundamental propagating TM mode in a sensing waveguide, α is the attenuation constant, β is the phase constant, $A = \alpha d$, $B = \beta d$ and a and b are real and imaginary parts of r_2^2 , respectively. In Eqs. (4)-(8), $|t_1 t_2|$ can be further calculated as $|t_1 t_2| = \sqrt{T_1 T_2 \frac{\text{Re}\{\gamma_1 \varepsilon_2\} \int |\phi_1|^2 dx}{\text{Re}\{\gamma_2 \varepsilon_1\} \int |\phi_2|^2 dx}}$. Here T_1 and T_2 are the power transmission coefficients at the input and output interfaces (Fig. 2), respectively, $\varepsilon_i (i = 1, 2)$ are complex dielectric constants of the input and output MDM waveguides, respectively, γ_i and $\phi_i (i = 1, 2)$ are complex wave vectors and field profiles of the fundamental TM modes in the input and output MDM waveguides, respectively. Due to the symmetry of all RI sensor structures considered in this paper, we have $|t_1 t_2| = \sqrt{T_1 T_2}$. Denoting $e^{-2A}(C_\alpha \frac{dA}{dn} + C_\beta \frac{dB}{dn}) = S_\gamma$, $e^{-2A}C_T \frac{d|t_1 t_2|^2}{dn} = S_T$ and $e^{-2A}(C_a \frac{da}{dn} + C_b \frac{db}{dn}) = S_R$, the *FOM* becomes

$$FOM = |S_\gamma + S_T + S_R|. \quad (10)$$

A and B are related to the effective index of the sensing waveguide, hence S_γ is named as the *index sensitivity coefficient*. $\frac{da}{dn}, \frac{db}{dn}$ and $\frac{d|t_1 t_2|^2}{dn}$ are factors associated with sensitivities of the reflection and transmission coefficients of the mode at the interfaces between MDM and sensing waveguides with respect to the RI variations. S_T and S_R will heretofore be referred to as the *transmission sensitivity coefficient* and *reflection sensitivity coefficient*, respectively. We note that η is a function of the reflection coefficient r_2 at sides of the sensing waveguide and also observe that factor $\frac{1}{\eta}$ exhibits a maximum when the Fabry-Perot resonance condition $2\arg(r_2) - 2\beta d = -2m\pi$ is satisfied, where m is an integer. Thus, C_α , C_β , C_a , C_b and C_T are factors associated with the Fabry-Perot resonances of the sensor structure. In addition, since A is directly related to the attenuation constant of the effective wave vector, the factor e^{-2A} is associated with the attenuation of the optical power in the sensing waveguide.

Figure 1(b) shows the *FOM* for the structure of Fig. 1(a) as a function of the sensing length d at operating wavelength $\lambda_0 = 1.55 \mu\text{m}$. For the range of length shown, the maximum

FOM (2.66) is obtained for such a structure at $d = 910$ nm (Fig. 1(b)). The FOM is computed directly by approximating the differential in Eq. (1) with the finite-difference formula $\frac{dT_{out}(n)}{dn} = \frac{T_{out}(n+\Delta n) - T_{out}(n-\Delta n)}{2\Delta n}$ [21, 30]. This approximation improves in accuracy as $\Delta n \rightarrow 0$. In the computations, we use $\Delta n = 10^{-4} \ll n_w$ [21]. Figure 1(b) also shows the FOM calculated using scattering matrix theory. It is observed that there is an excellent agreement between the scattering matrix theory results and the exact results obtained using FDFD. Thus, based on this analytical model, we can investigate the relative contributions of the three sensitivity coefficients to the overall RI sensitivity of the sensor (Eq. (10)).

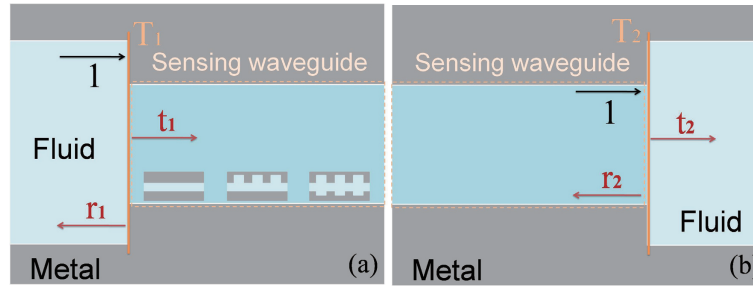


Fig. 2. (a) Schematic defining the reflection coefficient r_1 , transmission coefficient t_1 and power transmission coefficient T_1 when the fundamental TM mode of the input MDM waveguide is incident at the interface between the input and sensing waveguides. The sensing waveguides are a MDM waveguide, or a stub resonator system, or a double-stub resonator system (shown in the inset of Fig. 2(a)). (b) Schematic defining the reflection coefficient r_2 , transmission coefficient t_2 and power transmission T_2 when the fundamental TM mode of the sensing waveguide is incident at the interface between the sensing and output waveguides.

For the optimized MDM waveguide with small width sensor structure, the index sensitivity coefficient S_γ is -2.5686 (Table 1). We note the sensitivity $\frac{dB}{dn}$ (5.5068, Table 1) dominates over the sensitivity $\frac{dA}{dn}$ (0.0459, Table 1), which indicates the change in the phase constant of the mode induced by a RI variation is important in such a structure. On the other hand, the sensitivities $\frac{d|t_1 t_2|^2}{dn}$, $\frac{da}{dn}$ and $\frac{db}{dn}$ are -0.0404, 0.0130 and -0.0565 (Table 1), respectively, which means there are almost no relative changes in the power transmission and reflection of the sensing mode at the interface between MDM waveguides for a change in the RI of fluid, and therefore, the transmission sensitivity coefficient S_T (-0.0422, Table 1) and reflection sensitivity coefficient S_R (-0.0491, Table 1) are negligible.

2.2. MDM side-coupled to arrays of stub resonators system

To enhance the FOM , we next consider a plasmonic waveguide system consisting of a MDM waveguide side-coupled to a periodic array of stub resonators (stub-resonator system) [19] with stub width $w_1 = 50$ nm (Fig. 3(a)). N periods of the structure are included in the sensing region and the periodicity P is 150 nm. As before, the total length of the sensing structure is limited to less than $1.1 \mu\text{m}$, the widths w and w_0 are 140 nm and 50 nm, respectively. The group velocity of the optical mode in this system at a given wavelength can be tuned by adjusting the stub length L [19]. Figure 3(b) shows the FOM for the structure of Fig. 3(a) as a function of the stub length L and the number of periods N . For the range of parameters shown, we observe the optimized FOM of such a RI sensor structure obtained at $L = 150$ nm and $N = 3$ is 10.34, which is 3.9 times larger than that of the optimized MDM waveguide with small width system (2.66, Table 1). Figure 3(c) shows the first band of dispersion relation of the stub-resonator system.

We find such a system supports a slow-light mode for $L = 150$ nm at the operating wavelength of $\lambda_0 = 1.55$ μm . To investigate how the enhanced *FOM* actually depends on the slow light effect, the *FOM* can also be expressed as

$$FOM = \left| \frac{dT(\omega)}{dn} \right| = \left| \frac{dT(\omega)}{d\omega} \frac{d\omega}{dn} \right|. \quad (11)$$

where $d\omega$ is the spectral shift resulting from a small variation dn . Figure 3(d) shows the power transmissions of the sensing stub resonator system with $L = 150$ nm for $N=3$ and 4 obtained by FDFD. It is clear that there is no transmission when frequency is within the band gap (beyond 200 THz, Fig. 3(c)). In the vicinity of a resonance frequency ω_0 , the sensing stub resonator system is analogous to a photonic waveguide-cavity-waveguide system shown in the inset of Fig. 3(d) approximately [31]. Using coupled-mode theory (CMT) [9, 10, 31, 32], the energy amplitudes A , S_1^+ and S_2^- for the cavity, input and output waveguides can be described by

$$-i\omega A = -i\omega_0 A - \frac{A}{\tau_d} - \frac{A}{\tau_1} - \frac{A}{\tau_2} + \sqrt{\frac{2}{\tau_1}} S_1^+, \quad (12)$$

$$S_2^- = \sqrt{\frac{2}{\tau_2}} A. \quad (13)$$

Here $\frac{1}{\tau_d}$ is the decay rate due to the intrinsic loss, $\frac{1}{\tau_1}$ and $\frac{1}{\tau_2}$ are the decay rates into the input and output waveguides. Again, $\tau_1 = \tau_2$ by symmetry, and we denote the total decay rate into the input and output waveguides by $\frac{1}{\tau_w} = \frac{1}{\tau_1} + \frac{1}{\tau_2}$ (with quality factor $Q_w = \frac{\omega_0 \tau_w}{2}$) and the total decay rate by $\frac{1}{\tau} = \frac{1}{\tau_w} + \frac{1}{\tau_d}$ (with quality factor $Q = \frac{\omega_0 \tau}{2}$). Thus, the transmission spectrum can

be obtained by $T(\omega) = \left| \frac{S_2^-}{S_1^+} \right|^2 = \frac{\frac{1}{4Q_w^2}}{(\frac{\omega - \omega_0}{\omega_0})^2 + \frac{1}{4Q^2}}$, and the derivative $\frac{dT(\omega)}{d\omega}$ in Eq. 11 is

$$\frac{dT(\omega)}{d\omega} = \frac{\frac{\omega - \omega_0}{2\omega_0^2 Q_w^2}}{[(\frac{\omega - \omega_0}{\omega_0})^2 + \frac{1}{4Q^2}]^2}, \quad (14)$$

Moreover, the phase of the output propagating mode at the cavity/waveguide interface $\Phi(\frac{S_2^-}{S_1^+})$ is $\arctan(2Q\frac{\omega - \omega_0}{\omega_0})$. Thus, the group delay τ_g experienced by the propagating mode is given by

$$\tau_g(\omega) = \frac{d\Phi(\omega)}{d\omega} = \frac{\frac{2Q}{\omega_0}}{1 + [2Q(\frac{\omega - \omega_0}{\omega_0})]^2}, \quad (15)$$

At the resonance frequency ω_0 , the group delay is $\tau_g = \frac{2Q}{\omega_0}$. Substituting Eq. 15 into Eq. 14 gives $\frac{dT(\omega)}{d\omega} = 2(\omega - \omega_0)\tau_g^2(\omega)\frac{Q^2}{Q_w^2}$. In terms of $T(\omega_0) = \left| \frac{Q}{Q_w} \right|^2$, $\frac{dT(\omega)}{d\omega}$ further becomes $\frac{dT(\omega)}{d\omega} = 2(\omega - \omega_0)\tau_g^2(\omega)T_0$, where T_0 is $T(\omega_0)$. In the lossless case, $Q = Q_w$, $T(\omega_0) = 1$, and $\frac{dT(\omega)}{d\omega}$ reduces to $2(\omega - \omega_0)\tau_g^2(\omega)$. Note that the group velocity v_g of the propagating mode is inversely proportional to the group delay τ_g . Now, we have the following relationship

$$\frac{dT(\omega)}{d\omega} \sim \frac{T_0}{v_g^2(\omega)}(\omega - \omega_0), \quad (16)$$

On the other hand, in the vicinity of resonance frequency ω_0 , the rate of spectral shift $\frac{d\omega}{dn}$ in Eq. 11 is the same as the rate of shift of the resonance frequency approximately [33], that is,

$\frac{d\omega}{dn} \simeq \frac{d\omega_0}{dn}$. For the resonance closest to the band gap (slow light resonance, i.e., P_1, P_2 in Fig. 3(d)), $\beta(\omega_0) \simeq \frac{\pi}{P}$ as shown in Fig. 3(c) [19]. Thus, we have

$$\frac{d\omega}{dn} \simeq \frac{d\omega_0}{dn} \simeq \frac{\omega_0}{n}, \quad (17)$$

where n is the effective index of sensing waveguide. The derivative $\frac{d\omega_0}{dn}$ only depends on material parameters [33]. Combining Eqs. (16) and (17), Eq. (11) becomes

$$FOM = \left| \frac{dT(\omega)}{d\omega} \frac{d\omega}{dn} \right| \sim \left| \frac{T_0 \omega_0}{n v_g^2(\omega)} (\omega - \omega_0) \right|. \quad (18)$$

It is shown that the FOM is inversely proportional to the square of the group velocity v_g . That is, for a given frequency ω , the FOM increases as the group velocity v_g of the optical mode decreases due to the enhanced light-matter interactions.

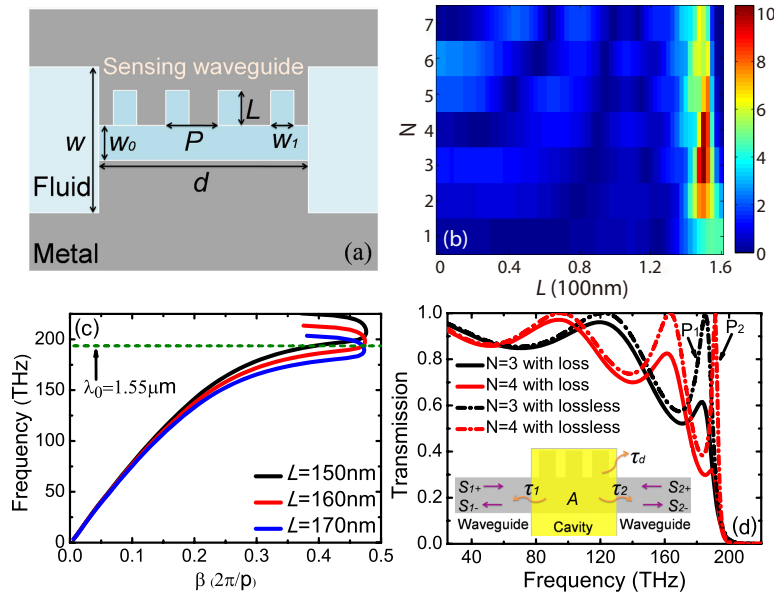


Fig. 3. (a) Schematic of the plasmonic RI sensor structure consisting of a stub resonator system sandwiched between two MDM waveguides. (b) FOM for the structure of Fig. 3(a) as a function of the stub length L and the number of periods N of the sensing system. Results are shown for $\lambda_0 = 1.55 \mu\text{m}$, $P = 150$ nm, $w_0 = w_1 = 50$ nm and $w = 140$ nm. (c) Dispersion relations of the stub resonator system for stub length $L = 150$ nm, 160 nm and 170 nm. All other parameters are as in Fig. 3(b). (d) Equivalent photonic waveguide-cavity-waveguide CMT model (shown in the inset of Fig. 3(d)) and power transmissions for the stub resonator system with $L = 150$ nm for $N = 3$ and 4 . All other parameters are as in Fig. 3(c).

In Fig. 3(d), we observe that the overlap between two adjacent resonance peaks due to a strong cavity-waveguide coupling leads that the lineshape of a peak (particularly, a peak with a resonance frequency far from the band gap) to some extent departs from a Lorentzian. Note that the key assumption for the CMT is weak coupling. In practice, it is typically found that the CMT is to be nearly exact for $Q \geq 30$ (i.e., the quality factors of slow light resonance peaks P_1 and P_2 (Fig. 3(d)), but also often qualitatively accurate for smaller Q [31]. Figure 3(d) shows

that the on resonance transmission coefficient is unity when the metallic loss is not included, as predicted from the CMT. A slow light resonance (high τ_g) results in light being "trapped" in the cavity for a longer duration which results in a weaker cavity-waveguide coupling and a higher Q (narrower spectral width of resonance, Fig. 3(d)) and thus higher light-matter interactions. This is consistent with the equation $\tau_g(\omega_0) = \frac{2Q}{\omega_0}$ obtained by the CMT as well. In addition, although the metal loss causes a power penalty relative to lossless case, the basic dependence in $\frac{T_0}{v_g^2}$ (Eq. 18) still holds. Thus, the enhancement in *FOM* of the stub-resonator system here is an outcome of the slow-light effect. Based on scattering matrix theory, we next investigate how the slow-light effect affects the sensitivities ($\frac{dA}{dn}, \frac{dB}{dn}, \frac{d|t_1 t_2|^2}{dn}, \frac{da}{dn}, \frac{db}{dn}$), attenuation factor e^{-2A} , and therefore the *FOM* of such sensor system by adjusting stub length L .

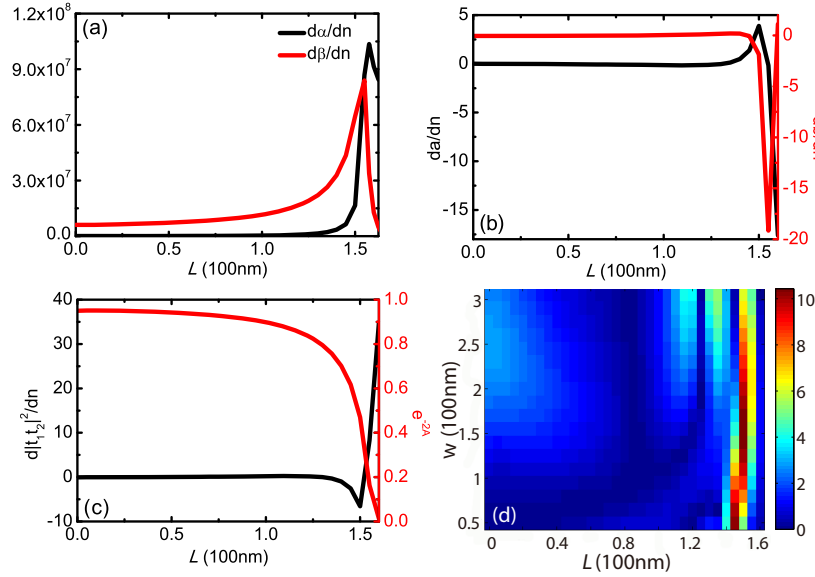


Fig. 4. (a) Sensitivities $\frac{d\alpha}{dn}$ (black line) and $\frac{d\beta}{dn}$ (red line) of the stub-resonator system in structure of Fig. 3(a) as a function of the stub length L . All parameters are as in Fig. 3(b). (b) Sensitivities $\frac{da}{dn}$ (black line) and $\frac{db}{dn}$ (red line) of the stub-resonator system in structure of Fig. 3(a) as a function of the stub length L . All parameters are as in Fig. 4(a). (c) Sensitivity $\frac{d|t_1 t_2|^2}{dn}$ (black line) and factor e^{-2A} (red line) of the stub-resonator system in structure of Fig. 3(a) as a function of the stub length L . All parameters are as in Fig. 4(a). (d) *FOM* for the structure of Fig. 3(a) as a function of the stub length L and the width w of the input and output MDM waveguides. All other parameters are as in Fig. 4(a).

Figure 4(a) shows the sensitivities $\frac{d\alpha}{dn}$ and $\frac{d\beta}{dn}$ of the stub resonator system in structure of Fig. 3(a) as a function of the stub length L for optimized $N=3$. We find as L increases, both sensitivities $\frac{d\alpha}{dn}$ and $\frac{d\beta}{dn}$ first increase, and then decrease after a specific length L . More specifically, the sensitivity $\frac{d\beta}{dn}$ achieves the maximum for $L = 155$ nm, and then decreases to zero. To explain this, in Fig. 3(c), we also display the first band of dispersion relations of the stub-resonator system for $L = 160$ nm and 170 nm, which exhibit band edge frequencies at 187 THz and 180 THz, respectively. As L increases, the band edge frequency of such system decreases, and as the operating frequency approaches the band edge frequency, the group velocity v_g decreases [19]. Thus, at the beginning, by increasing the stub length L from 0 to 155 nm, the sensitivity $\frac{d\beta}{dn}$ increases due to the slow-light enhanced light-matter interaction. However, as L further in-

creases, the group velocity begins to increase at $\lambda_0 = 1.55 \mu\text{m}$ (Fig. 3(c)), so the sensitivity $\frac{d\beta}{dn}$ decreases. When $L = 170 \text{ nm}$, the sensitivity $\frac{d\beta}{dn}$ even becomes negative because the dispersion relation experiences back-bending with negative group velocity at $\lambda_0 = 1.55 \mu\text{m}$ (Fig. 3(c)).

Table 1. Attenuation factor e^{-2A} , effective index sensitivities $\frac{dA}{dn}$, $\frac{dB}{dn}$, transmission sensitivity $\frac{d|t_1 t_2|^2}{dn}$, reflection sensitivities $\frac{da}{dn}$, $\frac{db}{dn}$, Fabry-Perot factors C_α , C_β , C_a , C_b , C_T , index sensitivity coefficient S_γ , transmission sensitivity coefficient S_T , reflection sensitivity coefficient S_R and figure of merit FOM of sensors calculated using scattering matrix theory. Results are shown for the optimized systems of Figs. 1(a), 3(a), and 5(a), respectively.

	MDM	stub resonator	double-stub resonator
e^{-2A}	0.9017	0.4699	0.5194
$\frac{d\alpha}{dn}, \frac{dA}{dn}$	5.0485×10^4 , 0.0459	1.6570×10^7 , 7.4567	-1.0263×10^7 , -3.0789
C_α	-1.7371	-1.3627	-1.4956
$\frac{d\beta}{dn}, \frac{dB}{dn}$	6.0515×10^6 , 5.5068	6.4604×10^7 , 29.0718	9.7606×10^7 , 29.2818
C_β	-0.5028	-0.1073	0.1736
S_γ	-2.5686	-6.2406	5.0320
$\frac{d t_1 t_2 ^2}{dn}$	-0.0404	-6.5733	6.9367
C_T	1.1589	0.9381	0.9864
S_T	-0.0422	-2.8976	3.5539
$\frac{da}{dn}$	0.0130	3.8833	-4.0082
C_a	0.9221	-0.4053	-0.0798
$\frac{db}{dn}$	-0.0565	-1.8689	-0.8233
C_b	1.1764	0.5244	-0.7808
S_R	-0.0491	-1.2001	0.5000
FOM	2.6599	10.3383	9.0859

Figure 4(b) shows the sensitivities $\frac{da}{dn}$ and $\frac{db}{dn}$ of the stub-resonator system in structure of Fig. 3(a) as a function of the stub length L for optimized $N=3$. Recall that a and b are real and imaginary parts of r_2^2 , that is, $a = r_p^2 - r_a^2$ and $b = 2r_p r_a$. Here $r_2 = r_p + ir_a$ is the complex reflection coefficient of the fundamental sensing mode of the stub-resonator system at the output interface (Fig. 2(b)). The real and imaginal parts of this reflection coefficient r_p and r_a are associated with the phase change and attenuation of the reflected sensing mode at the output interface (Fig. 2(b)), respectively [36]. In Fig. 4(b), we find that the sensitivities $\frac{da}{dn}$ and $\frac{db}{dn}$ experience significant changes in the slow-light region. The reflection coefficient sensitivities $\frac{da}{dn}$ and $\frac{db}{dn}$ are directly related to the attenuation sensitivity $\frac{d\alpha}{dn}$ and phase sensitivity $\frac{d\beta}{dn}$, respectively. When $L \leq 150 \text{ nm}$, as the group velocity decreases, the slow light effect leads to an enhancement in both sensitivities $\frac{db}{dn}$ and $\frac{da}{dn}$. Moreover, since the difference $\frac{d\beta}{dn} - \frac{d\alpha}{dn}$ is maximized at $L = 150 \text{ nm}$, so the maximum sensitivity $\frac{da}{dn} = \frac{dr_p^2}{dn} - \frac{dr_a^2}{dn}$ is also obtained at $L = 150 \text{ nm}$. When $150 \text{ nm} < L \leq 155 \text{ nm}$, as L increases $\frac{db}{dn}$ keeps increasing as a result of the group velocity decreasing (Fig. 4(a)). However, the difference $\frac{d\beta}{dn} - \frac{d\alpha}{dn}$ becomes smaller as L increases at this length range, so that $\frac{da}{dn}$ begins to decrease. Finally, when L increases beyond 155 nm, the group velocity begins to increase, so $|\frac{db}{dn}|$ rapidly decreases. In addition, $\frac{d\beta}{dn} - \frac{d\alpha}{dn} < 0$ leads to negative sensitivity $\frac{da}{dn}$, and as L increases, the difference $\frac{d\beta}{dn} - \frac{d\alpha}{dn}$ increases (Fig. 4(a)), therefore $|\frac{da}{dn}|$ increases as well.

Figure 4(c) shows the sensitivity $\frac{d|t_1 t_2|^2}{dn}$ of the stub-resonator system in structure of Fig. 3(a)

as a function of the stub length L for optimized $N=3$. We observe that sensitivity $\frac{d|t_1 t_2|^2}{dn}$ also experiences a significant enhancement as group velocity tuned by the stub length L . Note that $t_1 \simeq t_2$ due to reciprocity [36]. Thus, we obtain $|t_1 t_2|^2 \simeq |t_2^2|^2$. Since $|t_2^2|$ is approximated as $1 - |r_2^2|$ at the output interface (Fig. 2(b)), we have $\frac{d|t_1 t_2|^2}{dn} \simeq \frac{d|t_2^2|^2}{dn} \simeq \frac{d(1-|r_2^2|)^2}{dn}$. With the help of $r_2^2 = a + ib$, the sensitivity $\frac{d|t_1 t_2|^2}{dn}$ can be expressed as

$$\frac{d|t_1 t_2|^2}{dn} \simeq -2 \frac{1-|r_2^2|}{|r_2^2|} \left(a \frac{da}{dn} + b \frac{db}{dn} \right). \quad (19)$$

It is noted that the sensitivity $\frac{d|t_1 t_2|^2}{dn}$ is opposite but proportional to the sum of sensitivities $\frac{da}{dn}$ and $\frac{db}{dn}$ as shown in Fig. 4(c). Figure 4(c) also shows the attenuation factor e^{-2A} of the stub-resonator system in structure of Fig. 3(a) as a function of the stub length L for optimized $N=3$. As the stub length L increases, the operating frequency ($\lambda_0 = 1.55 \mu\text{m}$) approaches the band edge frequency, the field intensity in the stub resonators is enhanced, the real part of the wave vector increases, and therefore the attenuation of the sensing mode increases [19]. For large L , the decrease in the attenuation factor even dominates the increase in the slow-light enhanced sensitivity, so the mode with an extremely low group velocity may not always be the one that yields a high *FOM*. This is also consistent with Eq. (18) obtained by CMT. The *FOM* is not only inversely proportional to the square of the group velocity v_g , but also proportional to the resonance transmission T_0 . According to Eq. (3), the overall maximized *FOM* is thereby obtained for $L = 150 \text{ nm}$.

We find that for the optimized stub-resonator system the attenuation factor e^{-2A} is 0.47 (Table 1) which is 1.9 times smaller compared to that of the MDM waveguide with small width system 0.90 (Table 1). However, the absolute value of the sensitivities of the former system $|\frac{dA}{dn}|$, $|\frac{dB}{dn}|$, $|\frac{d|t_1 t_2|^2}{dn}|$, $|\frac{da}{dn}|$ and $|\frac{db}{dn}|$ are 7.46, 29.07, 6.5733, 3.8833 and 1.8689 (Table 1), which are 162.5, 5.3, 162.7, 298.7 and 33.1 times larger compared to those of the latter one (0.046, 5.51, 0.04, 0.013 and 0.057), respectively. Thus, the slow-light enhanced transmission sensitivity coefficient S_T (-2.9, Table 1), reflection sensitivity coefficient S_R (-1.2, Table 1) and attenuation sensitivity $\frac{dA}{dn}$ (-6.24, Table 1) cannot be neglected here. It is noted that the absolute value of factors C_α , C_β , C_T , C_a and C_b of the optimized stub-resonator system are all smaller than those of the MDM waveguide with small width system (Table 1), which indicates that the enhanced sensitivity coefficients of former system are not due to a better Fabry-Perot resonance condition matching. In addition, we observe that all factors C_α , C_β , C_T , C_a and C_b are functions of the attenuation factor e^{-2A} , therefore, the decrease in them is partly because of the increase in attenuation of the slow-light mode. Overall, the optimized slow-light enhanced stub resonator system (Fig. 3(a)) results in 3.9 times larger *FOM* compared to the optimized MDM waveguide with small width system (Fig. 1(a)). It is worth noting that $\frac{dT(n)}{dn}$ (Eq. (1)) can be positive or negative, which corresponds to increased or decreased power transmission, respectively, for a change in the RI. A good design for a sensing structure is to maximize such a variation in the power transmission. If all terms in Eq. (3), $C_\alpha \frac{dA}{dn}$, $C_\beta \frac{dB}{dn}$, $C_T \frac{d|t_1 t_2|^2}{dn}$, $C_a \frac{da}{dn}$ and $C_b \frac{db}{dn}$ have the same sign, a high *FOM* is achieved. Otherwise, they may cancel each other, and slow light enhanced sensitivities may decrease instead of increasing the overall *FOM*.

Since the MDM waveguides with different widths are used in various optical nanocircuits [26, 27, 34, 35], we also show the *FOM* for the structure of Fig. 3(a) as a function of the stub length L and width w of the input and output MDM waveguides for the optimized $N = 3$ (Fig. 4(d)). We note that the optimized stub length L is around 150 nm for any width, which suggests that the Fabry-Perot resonance effect here is less important than the slow-light effect. Due to the same reason, in Fig. 3(b), we observe that for different number of periods N , the corresponding

maximum FOM is always obtained around $L = 150$ nm as well.

2.3. MDM side-coupled to arrays of double-stub resonators system

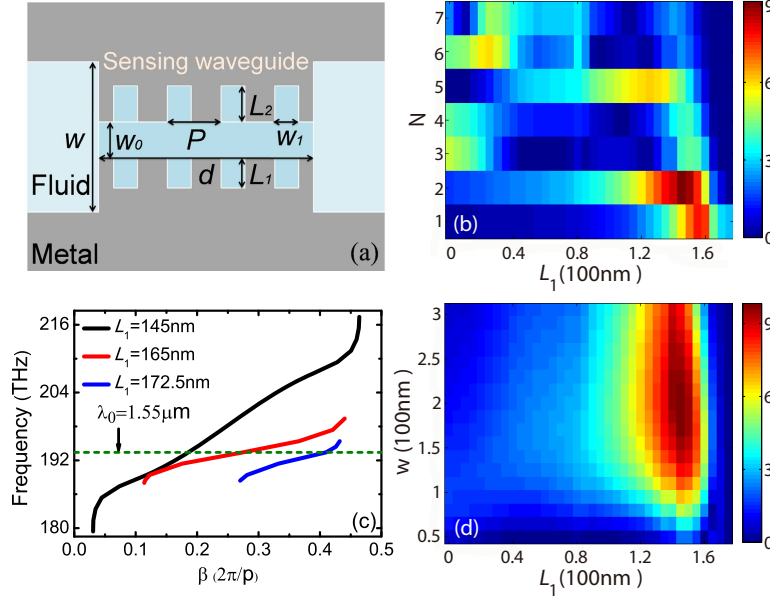


Fig. 5. (a) Schematic of the plasmonic RI sensor structure consisting of a double-stub resonator system sandwiched between two MDM waveguides. (b) FOM for the structure of Fig. 5(a) as a function of the stub length L_1 and the number of periods N of the sensing waveguide. All parameters are as in Fig. 3(b). (c) Dispersion relations of the slow-light waveguide based on a double-stub resonator system for stub length $L_1 = 145$ nm, 165 nm and 172.5 nm. All other parameters are as in Fig. 3(b). (d) FOM for the structure of Fig. 5(a) as a function of the stub length L_1 and the width w of the input and output MDM waveguides. All other parameters are as in Fig. 3(b).

We finally consider a slow-light plasmonic waveguide system consisting of a MDM waveguide side-coupled to arrays of double-stub resonators (double-resonator system) based on our previous work (Fig. 5(a)) [20], which was also implemented experimentally in a recent work [27]. Unlike the proposed MDM waveguide side-coupled to arrays of stub resonators system (Subsection 2.2), such a system can exhibit a small group velocity dispersion over a broad wavelength range, feature which is highly desirable for practical applications of slow-light devices [19, 20]. As before, the total length of the structure is limited to less than $1.1 \mu\text{m}$. The transmission spectra of such a double-stub resonator structure features a transparency peak centered at a frequency which is tunable through the length of the composite cavity formed by the two stub resonators $L_1 + L_2 + w_0$ [20]. Here we choose $L_1 + L_2 + w_0 = 420$ nm and $w_0 = 50$ nm, so that the transparency peak is centered at the operating frequency of $f = 194$ THz ($\lambda_0 = 1.55 \mu\text{m}$) approximately. Figure 5(b) shows the FOM for the structure of Fig. 5(a) as a function of the stub length L_1 and the number of periods N of the sensing waveguide system. For the range of parameters shown, the maximum FOM for such a RI sensor structure obtained at $L_1 = 145$ nm and $N = 2$ is 9.09, which is 3.5 times larger than that of the optimized MDM waveguide with small width system (2.66, Table 1). We also observe that increasing the number of periods N in the sensing region decreases the optimized stub length L_1 of the sensor. For a double-stub resonator system, as L_1 decreases, L_2 increases, since $L_1 + L_2 + w_0$ is fixed. Thus,

the stub length difference $\Delta L = L_2 - L_1$ increases, hence the frequency spacing between the stub resonances $\Delta\omega$ increases. As a result, the group velocity of the mode increases, and the corresponding propagation length and attenuation factor e^{-2A} increase as well [20]. When the number of periods N increases, the optimized stub length L_1 has to decrease to match this increase in the length of sensing region. Figure 5(c) shows the second band of dispersion relation of such sensing waveguide system, and we find the sensing waveguide supports a slow light mode for $L_1 = 145$ nm at $\lambda_0 = 1.55$ μm . As we discussed above, the 3.5 times enhancement is an outcome of the slow light effect. Figure 5(d) also shows the *FOM* for the structure of Fig. 5(a) as a function of the stub length L_1 and width w of the input and output MDM waveguides for optimized $N = 2$. Like the stub resonator system (Fig. 4(a)), we observe that for different width w , the corresponding maximum *FOM* is always obtained around $L_1 = 145$ nm as well. Again, we use single-mode scattering matrix theory to account for the behavior of the system.

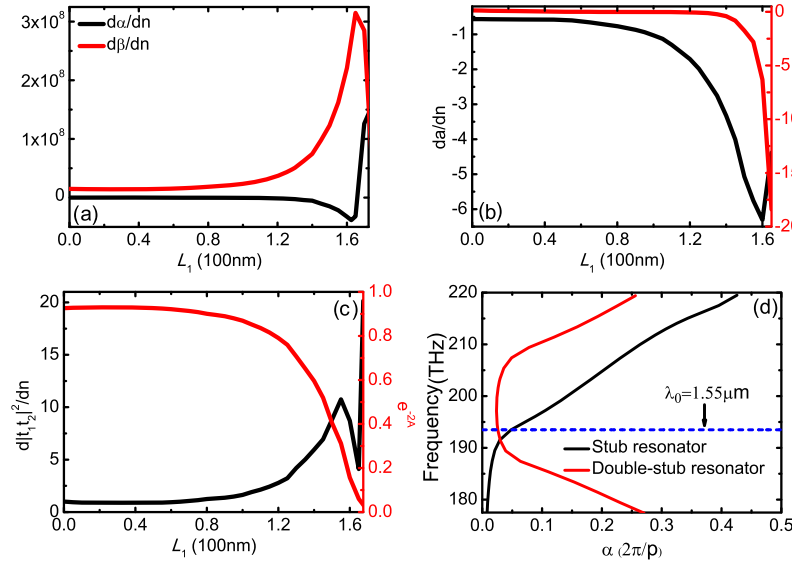


Fig. 6. (a) Sensitivities $\frac{d\alpha}{dn}$ (black line) and $\frac{d\beta}{dn}$ (red line) of the double-stub resonator system in structure of Fig. 5(a) as a function of the stub length L_1 . All parameters are as in Fig. 5(b). (b) Sensitivities $\frac{da}{dn}$ (black line) and $\frac{db}{dn}$ (red line) of the double-stub resonator system in structure of Fig. 5(a) as a function of the stub length L_1 . All parameters are as in Fig. 6(a). (c) Sensitivity $\frac{d|t_1t_2|^2}{dn}$ (black line) and factor e^{-2A} (red line) of the double-stub resonator system in structure of Fig. 5(a) as a function of the stub length L_1 . All parameters are as in Fig. 6(a). (d) Real part of the wave vector (attenuation constant) of the sensing mode α for the optimized stub resonator and double-stub resonator systems.

Figure 6(a) shows the sensitivities $\frac{d\alpha}{dn}$ and $\frac{d\beta}{dn}$ of the double-stub resonator system in structure of Fig. 5(a) as a function of the stub length L_1 for optimized $N=2$. A similar trend is seen: both $|\frac{d\alpha}{dn}|$ and $|\frac{d\beta}{dn}|$ first increase, and then decrease as L_1 further increases. The sensitivity $\frac{d\beta}{dn}$ is maximized when $L_1 = 165$ nm and then decreases to zero. To explain this, in Fig. 5(c) we display the second band of dispersion relations of the double-stub resonator system for $L_1 = 165$ nm and 172.5 nm. The stub length difference $\Delta L = L_2 - L_1$ decreases, the frequency spacing between the stub resonances $\Delta\omega$ decreases, hence the group velocity of the mode decreases [20]. As the stub length L_1 increases from 0 nm to 165 nm, the sensitivity $\frac{d\beta}{dn}$ increases due to the slow-light effect, As L_1 further increases to $L_1 = 172.5$ nm, the group velocity begins to

increase at $\lambda_0 = 1.55 \mu\text{m}$ (Fig. 5(c)), so the sensitivity $\frac{dB}{dn}$ decreases.

Figures 6(b) and 6(c) show the sensitivities $\frac{da}{dn}$, $\frac{db}{dn}$, $\frac{d|t_1 t_2|^2}{dn}$ and the attenuation factor e^{-2A} of the double-stub resonator system in structure of Fig. 5(a) as a function of the stub length L_1 for optimized $N=2$. The effect of slow-light on the performance of such a sensing system can be explained as in the case of the single-stub resonator system (Subsection 2.2).

We find that for the optimized double-stub resonator system the attenuation factor e^{-2A} is 0.52 (Table 1) which is 1.7 times smaller compared to that of the MDM waveguide with small width system (0.90, Table 1). However, like previously investigated stub resonator system, the absolute of sensitivities of the double-stub resonator system $|\frac{dA}{dn}|$, $|\frac{dB}{dn}|$, $|\frac{d|t_1 t_2|^2}{dn}|$, $|\frac{da}{dn}|$ and $|\frac{db}{dn}|$ (3.0789, 29.2818, 6.9367, 4.0082 and 0.8233, Table 1) are enhanced by the slow-light effect. The corresponding enhancements with respect to those of the MDM waveguide with small width system are 66.9, 5.3, 171.7, 308.3 and 14.4, respectively. We note that the absolute values of factors C_α , C_β , C_T , C_a and C_b of such a double-stub resonator system are not as large as those of the MDM waveguide with small width system, so the enhanced sensitivity coefficients S_T , S_R and S_γ (3.5539, 0.5000 and 5.0320, Table 1) of the double-stub resonator system are a result of the enhanced slow-light effect rather than of a Fabry-Perot resonance enhancement. We also observe that the *FOM* of the double-stub resonator system is slightly smaller than that of the stub resonator system just due to a smaller factor C_a (-0.0798, Table 1). Since the attenuation factors e^{-2A} of these two systems are comparable, so the sensitivity $\frac{da}{dn}$ of the double-stub resonator system has a worse Fabry-Perot resonance condition matching.

Table 2 summarizes the optimized design for each structure at operating wavelength $\lambda_0 = 1.55 \mu\text{m}$. The detection limit Δn_{min} is computed using Eq. (2) assuming input power of $P_{in} = 1 \text{ mW}$ and smallest measurable change in output power of $\Delta P_{out,min} = 10 \text{ nW}$ [21]. Based on the same equations (Eqs. (1) and (2)) and conditions ($P_{in} = 1 \text{ mW}$ and $\Delta P_{out,min} = 10 \text{ nW}$), Berini investigated the sensing performance of a generic Mach-Zehnder interferometer (MZI) implemented with plasmonic waveguides, such as metal-dielectric single interface waveguide, thin DMD waveguide (width of 20 nm) and thin MDM waveguide (width of 20 nm), at the operating wavelength $\lambda_0 = 1.31 \mu\text{m}$ [21]. The metal was gold and the dielectric also was water. The detection limits of these structures were 3.6×10^{-7} , 1.5×10^{-8} and 6.6×10^{-6} with optimal sensing lengths $d_e = 82.9 \mu\text{m}$, $2039 \mu\text{m}$ and $2.5 \mu\text{m}$, respectively. For a comparison, although the detection limits of the first two MZI based structures are 2.7 and 64.7 times smaller than that of the slow light enhanced stub resonator structure (9.7×10^{-7} , Table 2), the required sensing lengths of these two MZI based structures are 184.2 and 4531.1 times larger than that of the slow light enhanced stub resonator structure (450 nm, Table 2), respectively. In other words, these two structures are not suitable for ultradense chip-scale integration. In Table 2, we also observe that the slow-light enhanced sensors lead to not only 3.9 and 3.5 times enhancements in the detection limit, but also to 2 and 3 times reductions in the required sensing length, respectively, compared to the sensor using a MDM waveguide with small width structure. It is due to the fact that the slow light enhanced light-matter interactions can not only enhance the sensitivity, but can also greatly reduce the required sensing length, thereby enabling the realization of miniature sensors [37].

Finally, the power loss is of practical importance for application of plasmonic sensors. In Table 1, we observe that the attenuation factor e^{-2A} of optimized double-stub resonator system (0.5194) is higher than that of stub resonator system (0.4699) at $\lambda_0 = 1.55 \mu\text{m}$. In Table 2, it is also observed that the transmission of the former optimized system (0.363) is higher than that of the latter one (0.349). In Fig. 6(d), we show the real part of the wave vector (attenuation constant) as a function of frequency of the optical mode α for the optimized stub resonator and double-stub resonator systems. In the stub resonator system, the attenuation constant α greatly increases as the frequency approaches the band edge frequency. On the other hand, in the

double-stub resonator system the attenuation constant α is relatively small in the corresponding slow light frequency range (186 THz to 210 THz, Fig. 5(c)). Figure 6(d) demonstrates that the attenuation constant α in the double-stub resonator system is smaller than that in the single stub resonator system at the operating wavelength of $\lambda_0 = 1.55 \mu\text{m}$, in other words, the double-stub resonator system is less lossy. This is due to the fact that the composite cavity formed by two stubs in the double-stub resonator system has a weak resonance at a slow light wavelength such as $\lambda_0 = 1.55 \mu\text{m}$.

Table 2. Summary of waveguide designs and operating parameters at $\lambda_0 = 1.55 \mu\text{m}$. The optimal sensing lengths d_e , power transmission coefficients and detection limits Δn_{\min} of sensors are shown for the optimized systems of Figs. 1(a), 3(a), and 5(a), respectively.

	d_e	Transmission	Δn_{\min}
MDM	910nm	0.663	3.8×10^{-6}
stub resonator	450nm	0.349	9.7×10^{-7}
double-stub resonator	300nm	0.363	1.1×10^{-6}

3. Conclusions

In this paper, we investigated subwavelength scale slow-light enhanced RI sensors structures. In all cases, the total length of the structure was limited to less than $1.1 \mu\text{m}$, which approximately corresponds to one wavelength in water $\lambda_s = \lambda_0/n_w$, when operating at $\lambda_0 = 1.55 \mu\text{m}$. We first considered a structure consisting of a plasmonic MDM waveguide with small width sensing system sandwiched between two conventional MDM waveguides. To enhance the sensor performance, we next consider two other MDM waveguide based slow-light sensing systems: a MDM waveguide side-coupled to arrays of stub resonators (stub resonator) system and a MDM waveguide side-coupled to arrays of double-stub resonators (double-stub resonator) system. We found that, as the group velocity decreases, the sensitivity of the effective index of the mode to variations of the RI of the fluid increases and the sensitivities of the reflection and transmission coefficients of the mode to variations of the RI of the fluid at the interface between the MDM and sensing waveguides increase as well. The optimized slow-light enhanced sensors lead to not only 3.9 and 3.5 times enhancements in the RI sensitivity, and therefore in the minimum detectable RI change, but also 2 and 3 times reductions in the required sensing length, respectively, compared to the sensor using a MDM waveguide with small width system. Although the stub resonator system exhibits a slightly larger enhancement, the double-stub resonator system exhibits a small group velocity dispersion over a broader wavelength range, and its power loss is smaller. In addition, high power attenuation limits the performance of the slow-light enhanced plasmonic sensors. If gain and tunable RI materials are combined with these slow-light waveguides based sensors to compensate for the metallic loss [9, 20], they could enable stopping and storing light in a subwavelength volume, and could further lead to at least an order of magnitude enhancement in the RI sensitivity.

Acknowledgments

Y. H. acknowledges the support of the Postdoctoral Research Foundation of CSU. C. M. acknowledges the support given by National Natural Science Foundation of China under Grant numbers 61422506 and 11204141. G.V. acknowledges the support of the National Science Foundation (Award No. 1102301).